


## RESEARCH ARTICLE

# Interface Engineering of Fe-Loaded ZnO Nanostructures via Wet Impregnation and Hydrothermal Routes for Enhanced CO Selectivity in CO<sub>2</sub> Photoreduction

Haythem S. Basheer<sup>1</sup> | Mohit Yadav<sup>1</sup> | Ákos Szamosvölgyi<sup>1</sup> | Ádám Balog<sup>2</sup> | Csaba Janáky<sup>2</sup> | Anastasiia Efremova<sup>1</sup> | Janos Kiss<sup>1</sup> | András Sápi<sup>1</sup>  | Ákos Kukovecz<sup>1</sup> | Zoltán Kónya<sup>1,3</sup>

<sup>1</sup>Department of Applied and Environmental Chemistry, Interdisciplinary Excellence Centre, University of Szeged, Szeged, Hungary | <sup>2</sup>Department of Physical Chemistry and Materials Science, Interdisciplinary Excellence Centre, University of Szeged, Szeged, Hungary | <sup>3</sup>HUN-REN Reaction Kinetics and Surface Chemistry Research Group, University of Szeged, Szeged, Hungary

**Correspondence:** András Sápi (sapia@chem.u-szeged.hu)

**Received:** 10 September 2025 | **Revised:** 7 November 2025 | **Accepted:** 10 November 2025

**Keywords:** CO selectivity | interfaces | iron loading | photoreduction | wet impregnation

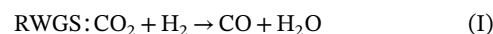
## ABSTRACT

This study reports the synthesis of iron-doped zinc oxide nanocomposites (ZnO-FeO<sub>x</sub>) via two distinct methods, hydrothermal (HT) and wet impregnation (WI), for photocatalytic CO<sub>2</sub> reduction under both visible light (VLI) and ultraviolet irradiation (UVI) light irradiation. The (HT) approach yielded a doped solid solution, whereas the (WI) method produced a heterosystem with well-defined interfaces. The ZnO-FeO<sub>x</sub> heterosystem demonstrated exceptional performance, achieving 99.99% selectivity for CO production with yields of 0.15 μmol g<sup>-1</sup> min<sup>-1</sup> (UVI) and 0.03 μmol g<sup>-1</sup> min<sup>-1</sup> (VLI). In comparison, the hydrothermally synthesized catalyst produced CO at yields of 0.042 μmol g<sup>-1</sup> min<sup>-1</sup> (UVI) and 0.006 μmol g<sup>-1</sup> min<sup>-1</sup> (VLI) with 94% selectivity. These results correspond to an approximately sevenfold enhancement for the WI-synthesized catalyst and a twofold improvement for the (HT) synthesized material relative to pristine ZnO. Combined surface analysis and DFT calculations showed that iron incorporation generates interfacial impurity states that facilitate a unique charge-transfer pathway, enhancing CO<sub>2</sub> photoreduction. DRIFTS confirmed formate and carbonyl species as key intermediates in the reaction mechanism.

## 1 | Introduction

Emulating natural photosynthesis, such as the photocatalytic reduction of CO<sub>2</sub> into reusable hydrocarbons using solar energy, presents quite a challenge. This process operates against thermodynamics, driving force [1–3]. The growing interest has focused on CO<sub>2</sub> recycling as a potential route to partially replace fossil oil by producing renewable carbon-based fuels through CO<sub>2</sub> conversion [4, 5]. Due to environmental concerns associated with CO<sub>2</sub>, researchers have shown significant interest in its conversion into value-added products. Various techniques have been explored, including photothermal catalysis, electrochemical conversion [6, 7]. However, the thermal reduction of CO<sub>2</sub> to produce CH<sub>4</sub> and CO typically requires substantial energy input and, in some cases, elevated pressures, resulting in high opera-

tional costs [8, 9]. The reversewater-gas shift (RWGS) reaction stands out as a promising strategy for CO<sub>2</sub> reduction to CO (Reaction 1):



CO plays a pivotal role as an intermediate in the production of value-added chemicals, particularly in industries using the Fischer-Tropsch (FT) process [10].

Zinc oxide (ZnO) offers the advantages of being nontoxic and cost-effective, making it an attractive candidate for photochemical applications. However, its relatively wide bandgap (~3.2–3.3 eV) restricts its photoresponse to the UV region (<400 nm), which constitutes only ~5–5.5% of the solar spectrum, significantly limiting its practical utilization. Consequently, this wide bandgap also

leads to fast electron recombination and photocatalytic corrosion. Therefore, strategies to reduce the electron fast recombination, charge separation, and extend light absorption into the visible region are of great interest [11, 12]. As a result, a strong interest to overcome the ZnO limitation (electron fast recombination, charge separation, and photo-corrosion), and enhancing the response to visible light. Researchers have explored various strategies, such as doping with metals or nonmetals, noble metal loading, and constructing heterojunctions, to broaden light absorption, create defect sites, and improve charge separation [13–19].

Recently, designing heterostructure catalysts that enhance charge separation and visible light response has emerged as a promising new approach, combining CO<sub>2</sub> reduction with simultaneous organic oxidation, generating valuable products on both ends without the need for sacrificial agents using Z-scheme CdSe/CdS systems and Pt/Zn<sub>0.75</sub>Cd<sub>0.25</sub>S has been reported [20–23].

Catalysts based on iron-loaded ZnO, produced using wet impregnation, have demonstrated the ability to effectively capture electrons. This capability suppresses the recombination of photo-generated electron–hole pairs, ultimately enhancing photocatalytic activity. The deposition of noble metals onto ZnO surfaces has also been reported for CO<sub>2</sub> photoreduction. According to the literature, Fe-doped ZnO can enhance photocatalytic activity at an optimized doping ratio in the (UVI) region. It also increases activity in the visible region; however, excessive doping leads to the formation of a secondary phase, ZnFe<sub>2</sub>O<sub>4</sub> [24]. In this research, we focused on the incorporation of iron into ZnO using two strategies (WI) and (HT) to investigate the changes that occurred, which leads to enhancing the photocatalytic efficiency and tune the selectivity of ZnO toward CO via photo-reduction of CO<sub>2</sub>.

## 2 | Experimental

### 2.1 | Material

#### 2.1.1 | Chemicals

The chemicals used in this study were of analytical grade and were used directly without additional purification. Zinc nitrate hexahydrate (Zn(NO<sub>3</sub>)<sub>2</sub> · 6H<sub>2</sub>O, 99%) and iron(III) nitrate nonahydrate (Fe(NO<sub>3</sub>)<sub>3</sub> · 9H<sub>2</sub>O, 99%) were sourced from Sigma–Aldrich. Citric acid (analytical reagent grade, 99.5%), absolute ethanol (99.8%) (Molar Chemicals), and Milli-Q water were used in the synthesis. For photocatalytic testing, a CO<sub>2</sub>:H<sub>2</sub> gas mixture with a 1:2 ratio (Messer) was used.

### 2.2 | Synthesis of Iron-Loaded Zinc Oxide Catalysts

#### 2.2.1 | Synthesis of Iron-Loaded ZnO by the HT Method

A hydrothermal technique adapted from the literature was used to synthesize the catalysts [25]. A typical synthesis began by dissolving 0.1 M Zn(NO<sub>3</sub>)<sub>2</sub> · 6H<sub>2</sub>O in 100 mL of water under continuous stirring. Citric acid (CA) was added to this solution after ten minutes. Upon complete dissolution, a 2 M NaOH solution was slowly added to adjust the pH to 12, forming a white aqueous suspension. This suspension was sealed within Teflon-lined stainless-steel autoclaves and heated at 160°C for 20 h. Doping was achieved by adding Fe(NO<sub>3</sub>)<sub>3</sub> · 9H<sub>2</sub>O at concentrations

between 0.002 and 0.01 M, calculated based on the molar ratio of the zinc precursor. The solid products obtained were purified by centrifugation, washed with distilled water and ethanol, and dried at 80°C. The final step involved calcining the bare ZnO (HT) samples at 500°C for 2 h under an air atmosphere.

#### 2.2.2 | Synthesis of Iron-Loaded ZnO by the WI Method

Catalysts with iron loadings of 2–10 wt% (ZnO–FeO<sub>x</sub>) were prepared using a wet-impregnation (WI) method. ZnO powder was dispersed in an aqueous solution of Fe(NO<sub>3</sub>)<sub>3</sub> · 9H<sub>2</sub>O and subjected to ultrasonication for 1 h. The material was then dried in an oven at 80°C. To remove nitrate species, the impregnated samples were subsequently calcined at 500°C for 3 h under a limited oxygen environment.

### 2.3 | Characterization

X-ray diffraction (XRD) analysis was conducted on a Rigaku Miniflex-II diffractometer using Ni-filtered Cu K $\alpha$  radiation ( $\lambda = 1.54 \text{ \AA}$ ), operating at 30 kV and 15 mA. X-ray photoelectron spectroscopy (XPS) measurements were performed on a Specs instrument equipped with an XR50 dual-anode X-ray source and a Phoibos 150 hemispherical electron analyzer. The Al K $\alpha$  source operated at 150 W (14 kV). Survey spectra were acquired at 40 eV pass energy with a 1 eV step size, while high-resolution spectra were collected at 20 eV pass energy with 0.1 eV energy resolution. All high-resolution spectra were charge-referenced to the aliphatic carbon C1s peak at 284.8 eV. Shirley background subtraction was applied uniformly to all spectra. Morphological characterization was performed using an FEI TECNAI G2 20 X-Twin high-resolution transmission electron microscope (TEM). Raman spectroscopy was conducted on a Horiba Scientific LabRAM HR-800 laser Raman spectrometer. Diffuse reflectance infrared Fourier transform spectroscopy (DRIFTS) measurements were performed using an Agilent Cary-670 FTIR spectrometer equipped with a Harrick Praying Mantis diffuse reflectance accessory featuring BaF<sub>2</sub> windows. Following pretreatment (Section 2.4), samples were cooled to room temperature under helium flow before collection of the background spectrum. The CO<sub>2</sub>:H<sub>2</sub> mixture (1:2) was introduced at a total flow rate of 15 mL min<sup>-1</sup> at room temperature, followed by UV irradiation for timed intervals (1, 5, 10, and 20 min). External heating was applied to prevent condensation. Spectra were recorded from 4000 to 900 cm<sup>-1</sup> at 2 cm<sup>-1</sup> resolution, typically averaging 32 scans. The short optical path length in the DRIFTS cell minimized gaseous reactant contributions. Kelvin probe microscopy measurements were carried out using a KP Technology APS04 instrument. First, the Fermi level of the gold-alloy-coated tip was determined relative to a silver reference sample ( $E_{\text{Fermi}}$ , Au tip = 4.49 eV). The contact potential difference (CPD) was then measured between the tip and the samples (prepared by drop-casting on FTO) after reaching electrical equilibrium. During measurement, the 2-mm-diameter tip vibrated above the sample surface at a constant height (~1 mm), amplitude (0.2 mm), and frequency (70 Hz). The CPD value reflects the potential difference required to equalize the Fermi levels of the two materials; thus, knowing the Fermi level of the tip enables calculation of the sample Fermi level. The CPD was measured at three different positions

for each sample, and the error bars represent the standard deviation from the average.

## 2.4 | Photocatalytic CO<sub>2</sub> Reduction Performance

CO<sub>2</sub> hydrogenation photocatalytic activity was evaluated in a batch reactor composed of concentric glass cylinders (outer: 10.2 cm diameter × 25 cm height; inner: 6.4 cm diameter × 25 cm height). UV irradiation was supplied by an 11 W mercury vapor lamp (Heraeus Noblelight TQ 718,  $\lambda_{\text{max}} = 254$  nm) and visible light by an 11 W LED lamp (OSRAM DULUX D,  $\lambda \geq 420$  nm). Light intensity at the catalytic surface was measured using an Apogee MQ-200 Quantum Meter, yielding 283  $\mu\text{mol m}^{-2} \text{s}^{-1}$  (visible) and 40  $\mu\text{mol m}^{-2} \text{s}^{-1}$  (UV). Catalysts (250 mg) were suspended in 10 mL of absolute ethanol by ultrasonication and coated onto the outer surface of the inner cylinder. Pretreatment involved heating to 250°C with sequential gas exposures: Ar (20 min), O<sub>2</sub> (30 min), Ar (10 min), and H<sub>2</sub> (60 min). The reactant gas (CO<sub>2</sub>:H<sub>2</sub> = 1:2) was introduced between the cylinders using an Aalborg mass-flow controller, with continuous recirculation between the reactor and a gas chromatograph (HP 5890 Series II) via a pump system. Temperature was controlled using a cooling-water circulator. Product separation was achieved using a 2-m capillary column ( $d = 0.635$  cm) packed with Porapak QS polymer, with detection via flame-ionization and thermal-conductivity detectors.

## 2.5 | Theoretical Study

The Burai module of the open-source Quantum ESPRESSO software package was used for quantum mechanical modeling of materials. All calculations were performed using spin-polarized density functional theory (DFT) with the Perdew–Burke–Ernzerhof (PBE) functional under the generalized gradient approximation (GGA) for the exchange-correlation term. A Hubbard U correction of 7.5 eV was applied to both Zn and O atoms, and the plane-wave energy cutoff was set to  $2.5 \times 10^2$  Ry [26].

## 2.6 | Apparent Quantum Efficiency (AQE) Calculation

The AQE for photocatalytic CO<sub>2</sub> reduction to CO was calculated as Equation (1)

$$\text{AQE} = \frac{2 \times N_{\text{CO}}}{N_{\text{photons}}} \times 100 \quad (1)$$

where  $N_{\text{CO}}$  is the Number of CO molecules produced per  $\text{s}^{-1}$ , calculated by Equation (2)

$$N_{\text{CO}} = R_{\text{CO}} \times t \times N_{\text{A}} \quad (2)$$

where  $R_{\text{CO}}$  in  $\text{mol s}^{-1}$ ,  $t$ : Irradiation time (seconds),  $N_{\text{A}}$ : Avogadro's constant ( $6.022 \times 10^{23} \text{ mol}^{-1}$ ).

$N_{\text{photons}}$ : number of incident photons per second, calculated by Equation (3)

$$N_{\text{photons}} = \frac{P \times t \times \lambda}{hc} \quad (3)$$

where  $P$ : Total incident light power (W),  $\lambda$ : Wavelength of light (254 nm for UV, 420 nm for visible);  $h$ : Planck's constant ( $6.626 \times 10^{-34} \text{ J} \cdot \text{s}$ ),  $c$ : speed of light ( $3 \times 10^8 \text{ m} \cdot \text{s}^{-1}$ ) [27].

## 3 | Results and Discussion

### 3.1 | Results

#### 3.1.1 | Crystallographic Structure and Phase Purity Analysis

The crystalline structure and phase composition of the synthesized samples were assessed via X-ray diffraction (XRD). As shown in Figure 1a,b, the diffraction patterns exhibit characteristic peaks indexed to the [002, 100, 101, 102, 110, 103, 112] and [203] crystallographic planes of hexagonal ZnO (JCPDS No. 36–1451) [28]. Incorporation of Fe into the ZnO lattice induces structural distortions and defects, attributable to the ionic radius mismatch between Zn<sup>2+</sup> (0.074 nm) and Fe ions, Fe<sup>2+</sup> (0.078 nm), and Fe<sup>3+</sup> (0.068 nm). With increasing Fe content, diffraction peaks shift toward higher angles, consistent with the substitution of Zn<sup>2+</sup> by the smaller Fe<sup>3+</sup> species, which is identified as the dominant oxidation state by XPS analysis Figure 1b,d [29]. A noticeable reduction in the intensity of the [101] peak is observed at higher doping levels, suggesting the introduction of lattice strain and dislocations, as well as a decline in overall crystallinity (Table 1). For Fe concentrations exceeding  $x = 0.04$ , secondary phases may begin to form. ZnO-FeO<sub>x</sub> through wet impregnation Figure 1a,c retains the phase structure with enhanced dispersion. This introduction of iron does not induce phase changes, except at higher loading levels. With higher Fe loading, particle size increases, coupled with slight macrostrain due to lattice mismatch between ZnO and iron oxides (Table 1).

Strain-induced peak broadening is fundamentally linked to the presence of crystal imperfections are related by Equation (4)

$$\varepsilon \approx \beta s / 4 \tan(\theta) \quad (4)$$

where  $\beta s$  denotes the FWHM.

The dislocation calculated by Equation (5)

$$\delta = 1/d^2 \quad (5)$$

where  $d$  is referred to primary crystalline size.

Furthermore, dislocation density-defined as the total length of dislocation lines per unit volume serves as an indicator of defect concentration within the material. This parameter was observed to increase with higher dopant concentrations [24, 30].

#### 3.1.2 | Microstructural Analysis Using (SEM) and (TEM) Microscopy

The surface features of the catalysts synthesized via (HT), route and (WI) routes, both pure ZnO and the 8% Fe (WI) samples, exhibited irregular pellet or flake-like shapes, with no significant morphological changes observed upon iron loading Figure 2a,b. In contrast, the hydrothermally synthesized 4% Fe-doped sample displayed notable morphological transformation, forming nanorod structures (Figure 2c). Elemental mapping confirmed a uniform distribution of Fe in both the Fe-ZnO 4% (HT) Figure S1(e-h) and the ZnO-FeO<sub>x</sub> 8% (WI) samples Figure S1(a-d). TEM analysis revealed lattice spacings of 0.26 nm corresponding to the

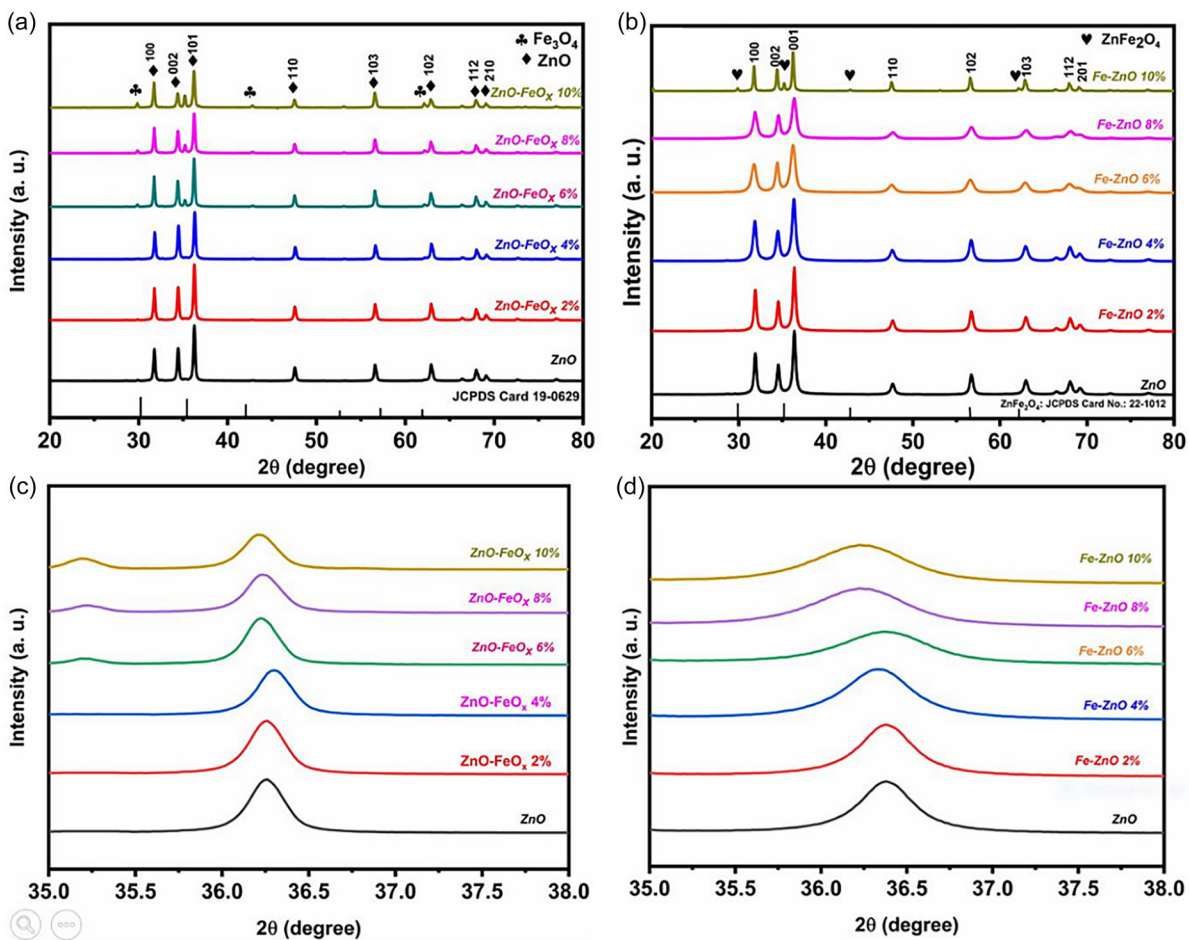


**FIGURE 1** | XRD patterns for (a) ZnO-FeO<sub>x</sub> (WI), (b) Fe-ZnO (HT), (c) zoomed 35°–38° range for ZnO-FeO<sub>x</sub> (WI), and (d) Zoomed 35°–38° range for Fe-ZnO (HI).

**TABLE 1** | Iron loading ZnO structural parameters.

Catalysts <sup>a</sup>	Hydrothermal			Wet impregnation		
	Primary particle size, nm	Microstrain · 10 <sup>-3</sup>	Dislocation · 10 <sup>-3</sup>	Primary particle size, nm	Dislocation · 10 <sup>-3</sup>	Microstrain · 10 <sup>-3</sup>
ZnO	33.84	1.0247	0.87325	33.84	0.87325	1.0247
ZnO-FeO <sub>x</sub> 2%	28.64	1.2331	1.21914	33.34	0.89964	1.1831
ZnO-FeO <sub>x</sub> 4%	24.92	1.3862	1.61029	34.83	0.82431	1.2262
ZnO-FeO <sub>x</sub> 6%	22.82	1.4526	1.9203	35.32	0.8016	1.2626
ZnO-FeO <sub>x</sub> 8%	19.33	1.674sn3	2.67631	35.98	0.77246	1.2798
ZnO-FeO <sub>x</sub> 10%	17.49	2.0826	3.26904	36.12	0.76649	1.2989

<sup>a</sup>The data illustrate the distinct structural impact of each synthesis method: (HT) Fe incorporation significantly reduces particle size and increases crystal defects (macrostrain and dislocation density), while the (WI) method maintains the ZnO microstructure with minimal perturbation, suggesting the formation of a surface FeO<sub>x</sub> phase.

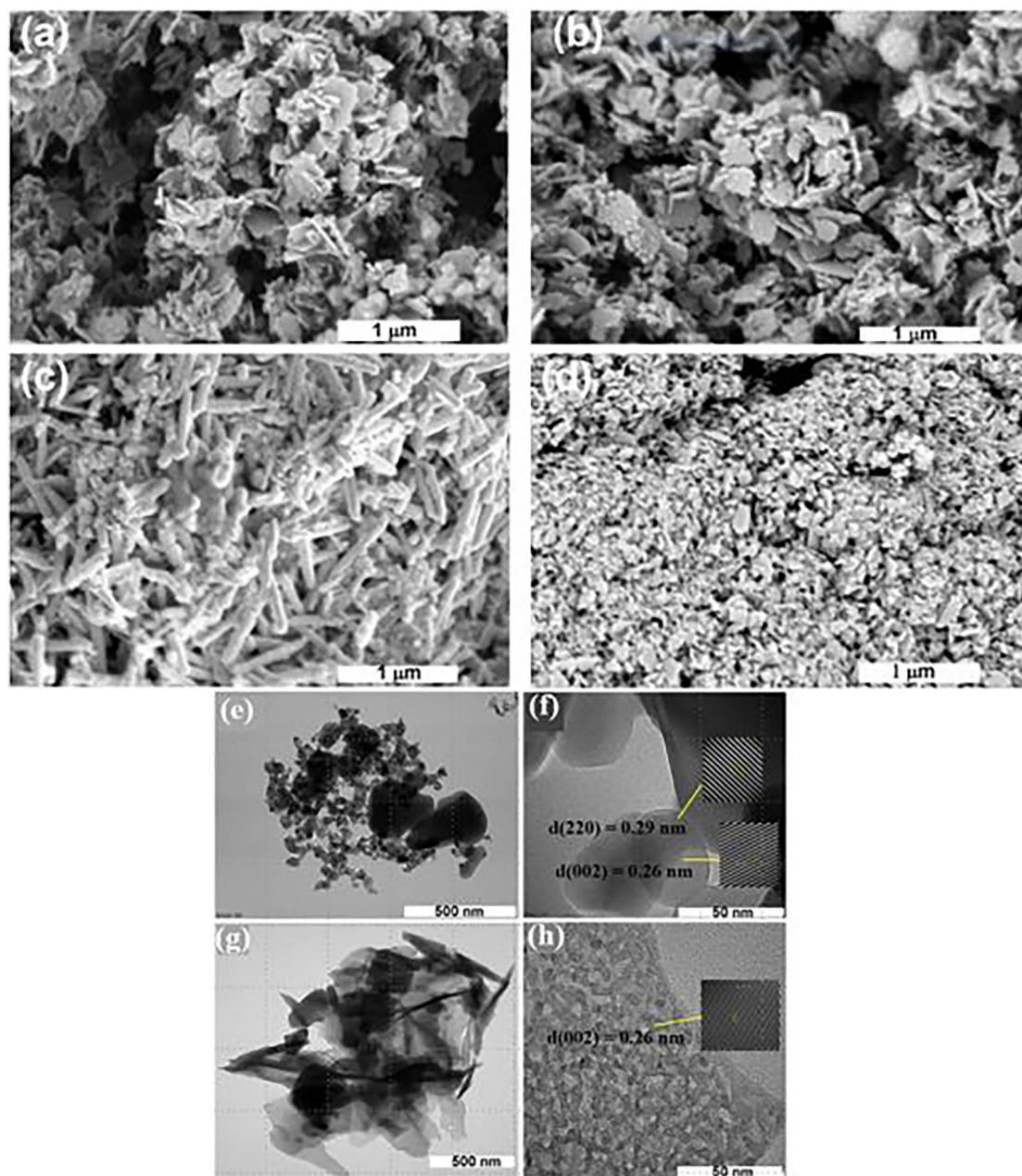


**FIGURE 2** | SEM images. (a) ZnO pure, (b) ZnO-FeO<sub>x</sub> 8% (WI), (c) Fe-ZnO 4% (HT), and (d) Fe-ZnO 10% (HT). TEM images for (e,f) ZnO-FeO<sub>x</sub> 8% & d spacing (WI) and (g,h) Fe-ZnO 4% (HT).

ZnO (002) plane and 0.29 nm to the Fe<sub>3</sub>O<sub>4</sub> (220) plane, confirming the formation of Fe<sub>3</sub>O<sub>4</sub> via the (WI) method (Figure 2e,f). In the Fe-ZnO 4% (HT) sample (Figure 2g,h), only the 0.26 nm (002) plane of ZnO was observed, indicating the absence of secondary phase formation, which was supported by the XRD results.

### 3.1.3 | Optical Properties and Raman Spectroscopy Analysis

Diffuse reflectance spectroscopy (DRS) Figure 3a,b revealed that pristine ZnO exhibits sharp absorption at 383 nm, corresponding to a 3.23 eV bandgap, attributed to intrinsic band edge absorption [31]. Figure 3a shows that the Fe-ZnO samples prepared using the hydrothermal method exhibited a broad absorption with a

shoulder at 600–652 nm [32]. This feature is due to Fe doping and the formation of ZnFe<sub>2</sub>O<sub>4</sub>, as confirmed by XRD Figure 1b [32], and is consistent with DFT Figure S5, with the most significant bandgap narrowing appearing at 10% Fe-ZnO doping. Similarly, Fe loading by the (WI) method introduced mid-gap states, leading to additional absorption features and reduced bandgap Figure 3b. Bandgaps estimated by the Kubelka-Munk equation (Table S1) decreased with increasing Fe content.

Raman spectroscopy Figure 3a,b revealed a strong E<sub>2</sub>-high mode at (437 cm<sup>-1</sup>), characteristic of defect-free ZnO [33]. Additional observed modes included E<sub>2</sub>-low (101 cm<sup>-1</sup>), A<sub>1</sub>-(TO) (380 cm<sup>-1</sup>), and E<sub>1</sub>-(TO) (410 cm<sup>-1</sup>), which further confirm the structural integrity of the ZnO lattice and demonstrate sensitivity to doping and strain effects. The A<sub>1</sub>-(LO) mode, observed at (574 cm<sup>-1</sup>), corresponds to longitudinal optical phonon vibrations along

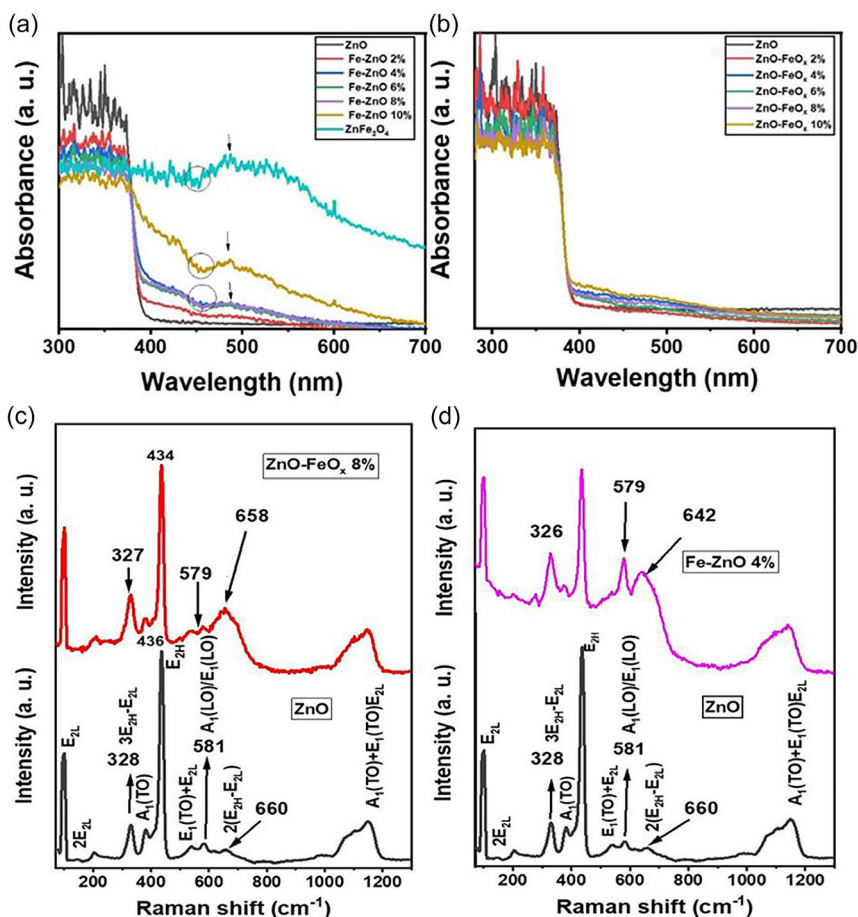


**FIGURE 3** | Diffuse reflectance spectra for (a) Fe-ZnO (HT), (b) ZnO-FeO<sub>x</sub> (WI) catalysts, (c) Raman shift for bare ZnO and iron loading samples using the (WI) method, and (d) (HT) method.

the c-axis and is particularly sensitive to the presence of free carriers (electrons) in ZnO. This mode is often used to study doping levels, as its position and width can shift or broaden depending on carrier concentration. For hydrothermally synthesized (HT) Fe-doped ZnO, Raman modes exhibit noticeable broadening, reduced intensity, and frequency shifts toward lower wavenumbers, as shown in Figure 3d [34]. These changes indicate disruptions in local symmetry, suggesting that Fe doping introduces new vibrational modes potentially due to the formation of Fe-O-Fe linkages or lattice distortions. In stark contrast, Figure 3c shows that the overall crystal structure of ZnO-FeO<sub>x</sub> synthesized via the (WI) method remains relatively intact at lower doping levels Figure S2. However, significant structural changes emerge at higher Fe loadings, particularly under (HT) doping at Fe-ZnO10%, as illustrated in Figure S3. At this concentration, a new peak appears around (639.56 cm<sup>-1</sup>), which is indicative of ZnFe<sub>2</sub>O<sub>4</sub> spinel formation [35].

Urbach energy ( $E_0$ ) serves as an indicator of the degree of structural disorder and defect concentration in a material. The value of  $E_0$  was determined by measuring the slope of the straight-line fit to the linear portion of the  $\ln(\alpha)$  vs.  $h\nu$  graph (Figure S9) (Equation 6).

$$E_0 = 1/m \quad (6)$$

where  $m$  is the slope.

Increased Urbach energy (Table S2) confirmed the introduction of defects, where the energy increased with higher doping amounts [36].

### 3.1.4 | XPS and Kelvin Probe Spectroscopy Evaluation

The survey for (WI) and (HT) was done using XPS (Figure 4). The oxidation state of iron was ascertained by analyzing the Fe 2p 3/2 peak. Due to a weak signal-to-noise ratio, multiple oxidation states could not be resolved in detail. The Fe species in the (WI) sample were identified as Fe<sub>3</sub>O<sub>4</sub> based on peak shape, with Fe 2p<sub>3/2</sub> located at 710.2 eV and Fe 2p<sub>1/2</sub> at 724.1 eV, features of Fe<sup>2+</sup>/Fe<sup>3+</sup> mixed states in Fe<sub>3</sub>O<sub>4</sub>. The Fe 2p<sub>3/2</sub> peak in Fe<sub>3</sub>O<sub>4</sub> is broader due to contributions from both Fe<sup>2+</sup> and Fe<sup>3+</sup>, as seen in Figure 4a [37]. In contrast, (HT) samples showed a sharper Fe 2p<sub>3/2</sub> peak at 711.0 eV (Table S3), indicating fully Fe<sup>3+</sup> with no satellite features (Figure 4b) [38]. The Zn 2p 3/2 binding energies are listed in Table S4. The modified Auger parameter ( $\alpha'$ ) confirmed Zn<sup>2+</sup> in the form of ZnO (Figure S4a,b). A 0.1 eV shift in Zn 2p 3/2 was observed in Fe-enhanced samples.

The Kelvin probe is used for the Fermi energy level determination. The Fermi level of pure ZnO was at -4.20 eV, which is very close to the conduction band typical n-type semiconductor. A significant downward shift of approximately 300 mV on the vacuum scale was observed for the Fe-doped ZnO compared to the pure material. Although this difference appears modest in the band diagram due to the wide bandgap, it is electronically substantial.

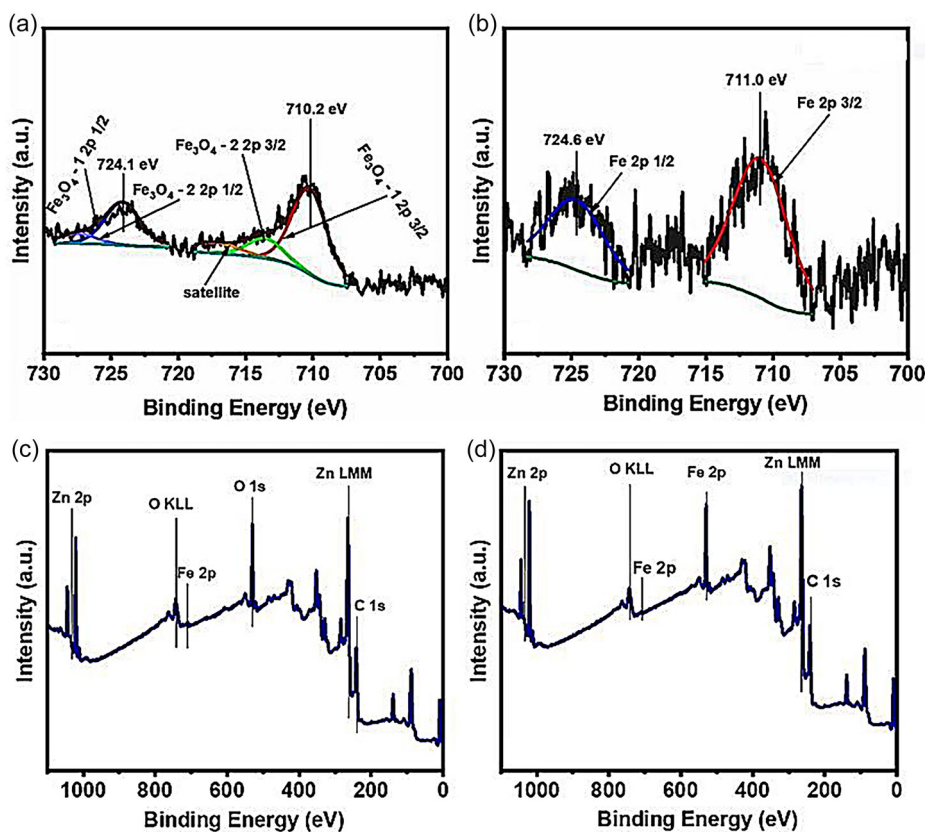


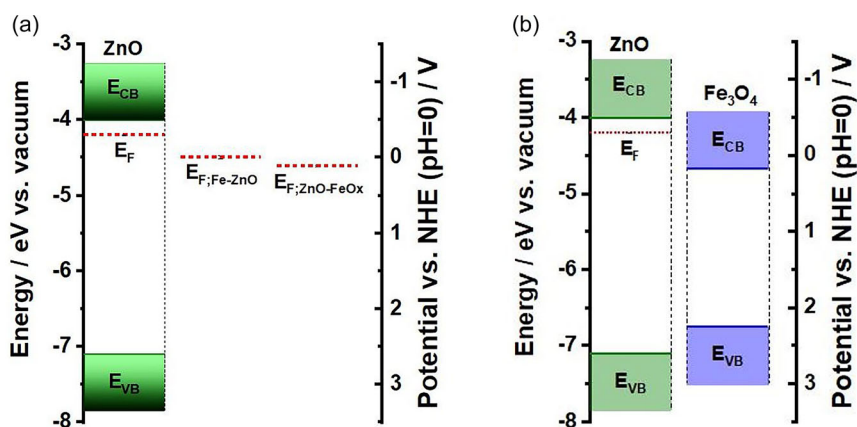
**FIGURE 4** | XPS spectra for Fe 2p (a) (WI), (b) (HT), and XPS survey for (c) (WI), and (d) (HT) samples.

The Fermi level of the ZnO-Fe<sub>x</sub>O<sub>y</sub> composite was found to be even more negative, shifted by an additional ~110 mV on the vacuum scale compared to Fe-doped ZnO (Figure 5a). Figure 5b illustrates the ZnO/Fe<sub>3</sub>O<sub>4</sub> band alignment, where ZnO (wide bandgap) couples with Fe<sub>3</sub>O<sub>4</sub> (narrow bandgap) to form a Type-II heterojunction. This alignment is beneficial for charge separation and transfer, making the composite material promising for photocatalysis or energy conversion applications.

### 3.1.5 | Results of the Photocatalytic CO<sub>2</sub> Reduction over the Iron-Loaded Zinc-Oxide

Photocatalytic CO<sub>2</sub> reduction tests (Table 2) showed that pristine ZnO was inactive under visible light but exhibited CO selective

photoreduction under (UVI) (0.021 (μmol g<sup>-1</sup> min<sup>-1</sup>)). Iron doping significantly improved efficiency, with Fe-ZnO 4% (HT) displaying the highest (UVI) activity (0.0422 (μmol g<sup>-1</sup> min<sup>-1</sup>)) and Fe-ZnO (HT) achieving the best visible light performance (0.006 (μmol g<sup>-1</sup> min<sup>-1</sup>)) (Figure 6a). The wet impregnated ZnO-FeO<sub>x</sub> catalyst showed remarkable activity and 99.99% CO selectivity (Figure S6), yielding (0.152 (μmol g<sup>-1</sup> min<sup>-1</sup>)) (UVI) and (0.030 (μmol g<sup>-1</sup> min<sup>-1</sup>)) (VLI) (Figure 6b). Stability tests confirmed consistent performance over five cycles (Figure S7). Furthermore, TGA was conducted before and after the photocatalytic test, which shows no detectable carbon loss, confirming complete organic removal before the catalytic test. Together, these results confirm that carbon residues are negligible and

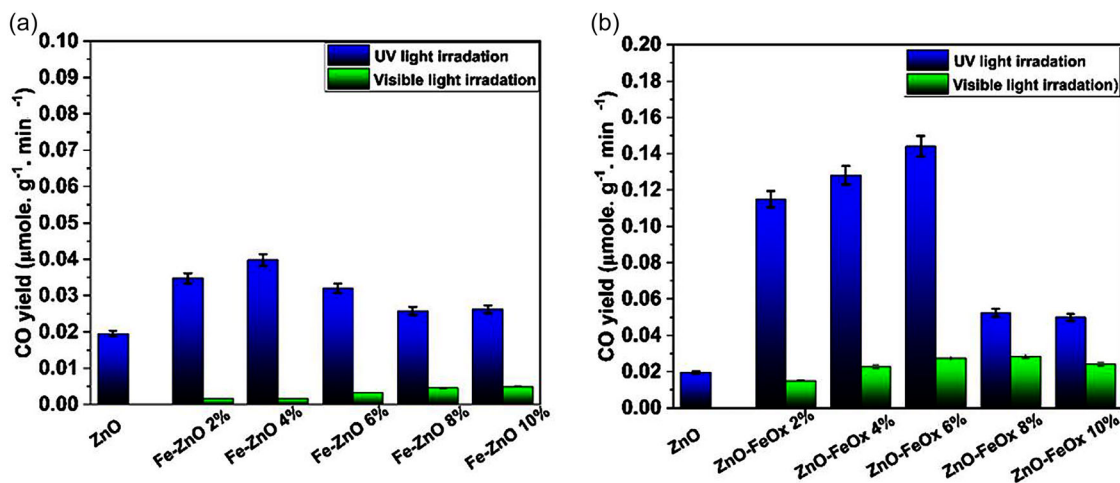


**FIGURE 5** | Kelvin probe spectroscopy determination of Fermi level and band alignment for (a) ZnO, Fe-ZnO 4% (HT), and ZnO-FeO<sub>x</sub> 8% (WI) and (b) ZnO-Fe<sub>3</sub>O<sub>4</sub>.

TABLE 2 | CO yield ZnO-iron loading samples.

Catalysts <sup>a</sup>	CO yield $\mu\text{mol g}^{-1} \text{min}^{-1}$ (WI) UV	CO yield $\mu\text{mol g}^{-1} \text{min}^{-1}$ (WI) Visible	CO yield $\mu\text{mol g}^{-1} \text{min}^{-1}$ (HT) UV	CO yield $\mu\text{mol g}^{-1} \text{min}^{-1}$ (HT) Visible
ZnO	0.0210	–	0.0210	–
ZnO-FeO <sub>x</sub> 2%	0.1220	0.0158	0.0368	0.0017
ZnO-FeO <sub>x</sub> 4%	0.1360	0.0242	0.0422	0.0018
ZnO-FeO <sub>x</sub> 6%	0.1520	0.0291	0.0340	0.0035
ZnO-FeO <sub>x</sub> 8%	0.0570	0.0302	0.0274	0.0049
ZnO-FeO <sub>x</sub> 10%	0.0530	0.0278	0.0260	0.0060

<sup>a</sup>The data demonstrates the superior photocatalytic performance of the (WI) synthesized catalysts, particularly at low to medium Fe loadings (2–8%), which achieve significantly higher CO yields under both UV and visible light compared to the (HT) samples.

FIGURE 6 | CO yield of CO<sub>2</sub> hydrogenation photocatalysis for (a) (HT) and (b) (WI) samples.

do not impact photocatalytic activity (Figure S8). A comparison with previously reported ZnO-based photocatalysts for CO<sub>2</sub> reduction under various conditions (Table S5) highlights an excellent CO yield and selectivity achieved by the ZnO-FeO<sub>x</sub> system.

## 3.2 | Discussion

### 3.2.1 | Bandgap Alignment

The electronic structure was initially evaluated using absolute electronegativity theory, an established method for predicting band alignment trends [39–41]. To validate these predictions, Kelvin probe measurements were performed (Figure 6). These measurements revealed a pronounced downward shift in the Fermi level following Fe incorporation, particularly in the (WI) ZnO-FeO<sub>x</sub> samples. This shift confirms that the synthesis method significantly governs the resultant electronic characteristics. The potentials of the Conduction band Minimum (CBM) and Valence band Maximum (VBM) were determined to elucidate the charge transfer mechanism pertinent to CO<sub>2</sub> reduction catalysis, using Equations (7) and (8)

$$E_{\text{CB}} = \chi - E_e - 0.5E_g \quad (7)$$

$$E_{\text{VB}} = ECB + E_g \quad (8)$$

where  $\chi$  is the absolute electronegativity of ZnO (5.8 eV);  $E_e = 4.5$  eV;  $E_g$  = bandgap energy [42].

Kelvin probe spectroscopy measurements revealed that the Fermi energy level (EF) for bare ZnO, which is located near its conduction band minimum (CBM), is consistent with its behavior as an n-type semiconductor [43]. In Fe-ZnO, a downshift in the Fermi level was observed, indicating electron withdrawal. This suggests that Fe doping introduces acceptor-like states, which act as surface electron traps. Further downshifting of the Fermi level in the ZnO-FeO<sub>x</sub> composite implies stronger charge separation and interfacial potential formation, likely due to the presence of Fe<sub>3</sub>O<sub>4</sub>, a mixed-valence oxide with its own electronic states Figure 6a,b.

A heterogeneous system is formed through the interaction between ZnO and FeO<sub>x</sub> (Fe<sup>2+</sup>/Fe<sup>3+</sup>), which creates a diverse array of active sites when FeO<sub>x</sub> is applied to ZnO through (WI). This process reveals surface defects, including oxygen vacancies and iron centers. To achieve optimal dispersion of FeO<sub>x</sub>, a loading of about 8% was selected, ensuring that it remained well distributed. This setup maximizes the contact area between ZnO and FeO<sub>x</sub>, which is essential for effective charge separation and the adsorption and activation of CO<sub>2</sub>. Under UV light excitation (Figure 7a), photogenerated electron-hole pairs are produced in ZnO. The electrons are

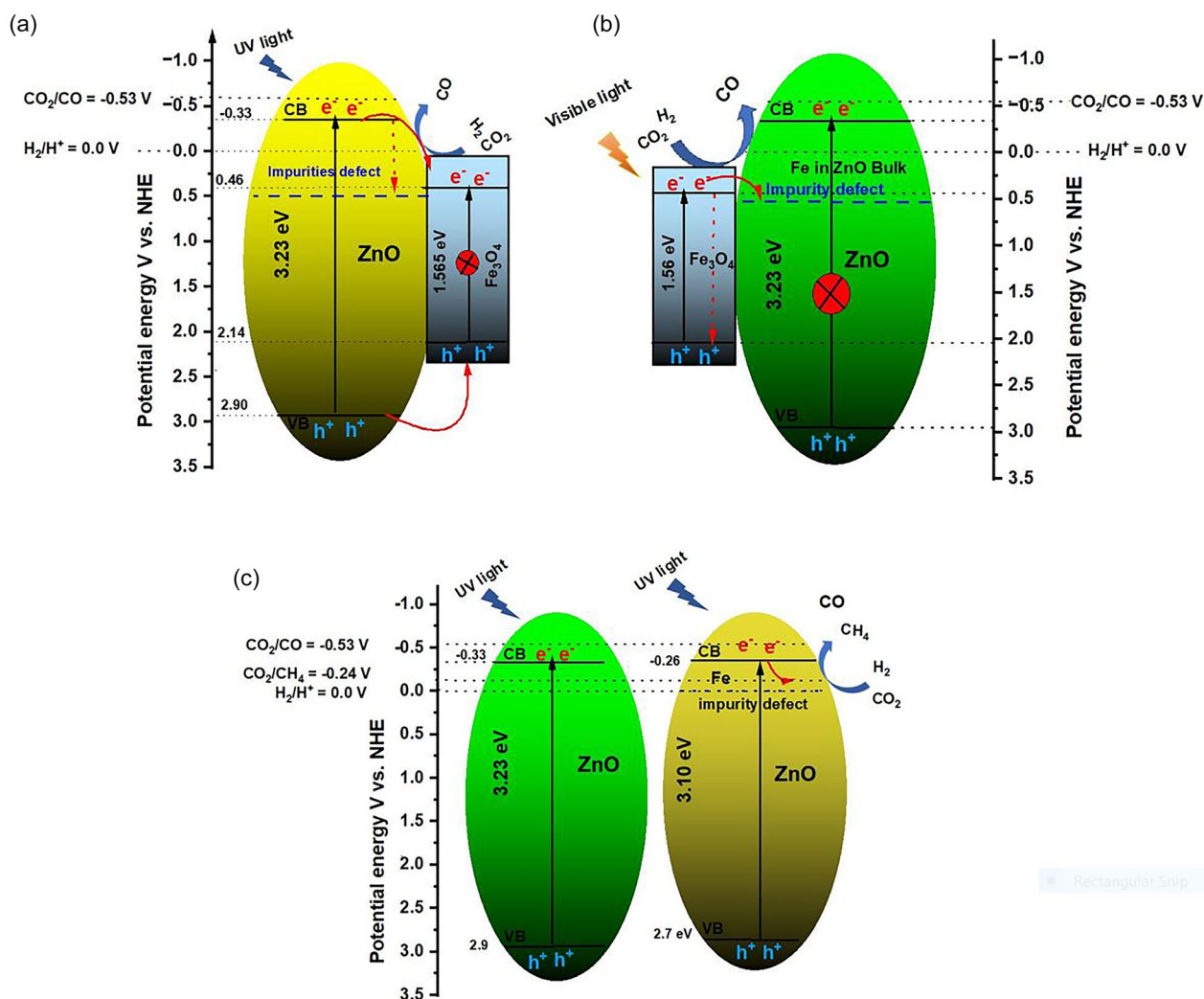


**FIGURE 7** | Schematic representation of band alignment for (a) ZnO-FeOx FeOx 8% (WI) (UVI), (b) ZnO-FeOx 8% (WI) (VLI), and (c) ZnO bare and Fe-ZnO (HT) (UVI).

subsequently transferred to  $\text{Fe}^{3+}$  centers on  $\text{Fe}_3\text{O}_4$ , where they are reduced to  $\text{Fe}^{2+}$ . This electron transfer minimizes electron-hole recombination, extending the lifetime of excited electrons and thereby enabling more efficient  $\text{CO}_2$  reduction. Meanwhile, the holes remain confined within the valence band of ZnO [39].

Under visible light, as shown in Figure 7b, while  $\text{Fe}_3\text{O}_4$  does absorb some visible light, the ZnO- $\text{Fe}_3\text{O}_4$  composites only show a slight increase in CO formation compare it to (UVI), measuring at just  $0.03 \mu\text{mol g}^{-1} \text{min}^{-1}$ . This modest enhancement is mainly due to the unfavorable band alignment between the two materials, which hinders the efficient transfer of electrons from  $\text{Fe}_3\text{O}_4$  to ZnO. Additionally, the strong electron-hole recombination within the ZnO system (with an energy gap of about 3.0–3.2 eV) means that the conduction band (CB) is negative enough to thermodynamically support the conversion of  $\text{CO}_2$  to CO (around  $-0.3$  to  $-0.5$  V vs. NHE). In contrast,  $\text{Fe}_3\text{O}_4$  has a more positive CB position around (0.48 V vs. NHE) and a very narrow bandgap (1.6 eV) [40]. Because of this, the photoexcited electrons produced in  $\text{Fe}_3\text{O}_4$  struggle to move efficiently to the ZnO CB, which is necessary for  $\text{CO}_2$  reduction. This unfavorable band offset results in poor charge transport at the interface, leading to minimal photocatalytic activity. Furthermore,  $\text{Fe}_3\text{O}_4$  is not a typical semiconductor with a

clear band structure because of it is spin polarization mixed valence metal; it has strongly localized d-electrons that promote rapid electron-hole recombination [41]. Consequently, the photogenerated carriers in  $\text{Fe}_3\text{O}_4$  do not last long enough to engage in surface redox reactions, which further reduces any potential sensitization effect on ZnO. As a result,  $\text{Fe}_3\text{O}_4$  mainly acts as a recombination center rather than an effective photosensitizer, which explains the low visible-light CO production seen in the ZnO- $\text{Fe}_3\text{O}_4$  composites. Additionally, the wet-impregnation process can introduce defects related to impurities that are crucial for boosting photocatalytic performance to some extent. These defects, particularly oxygen vacancies and Fe-related impurity states, help facilitate the movement of photogenerated electrons from ZnO to  $\text{Fe}_3\text{O}_4$ , acting as charge-trapping and transfer centers [39, 44]. Meanwhile, the photocatalytic reduction of  $\text{CO}_2$  over bare ZnO is limited by fast electron-hole recombination (Figure 7c). Incorporating Fe via (HT) synthesis introduces defect sites that trap electrons, enhancing charge separation and enabling more efficient  $\text{CO}_2$  conversion, producing mainly CO and small amounts of  $\text{CH}_4$ .

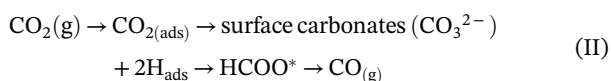
Recently, researchers have been working on improving ZnO-based photocatalysts for  $\text{CO}_2$  reduction, diving into dopants and heterojunction designs to reveal the best way to control light

absorbance, charge separation, and product selectivity. Some impressive results have been reported with Cu/Fe-doped ZnO nanorods and Co-doped ZnO nanoparticles, which have notably boosted CO yields due to the formation of impurity levels and improved charge transfer [45, 46]. Additionally, heterostructures such as p-n Co3O4/ZnO aerogels, S-doped ZnO QDs/g-C3N4, and Ag-Cu2O/ZnO nanorods have taken things a step further by enhancing CO2 adsorption, expanding light absorption, and facilitating interfacial charge transport [47, 48]. When we compare this to our Fe-modified ZnO, it shows about a 7-fold performance boost through wet impregnation and a 2-fold improvement with hydrothermal synthesis compared to standard ZnO (Table S5).

### 3.2.2 | Reaction Mechanism Determination Using DRIFTS

For understanding the in-depth mechanism of CO2 hydrogenation using as-fabricated ZnO-iron system photocatalysts (HT & WI), in situ DRIFTS were carried out to record the absorbance spectra and identify functional groups, as shown in Figure 8. The possible mechanisms for the CO2 reduction process, which occur in both Figure 8a (WI) and 8b (HT) catalysts as follows:

Direct CO2 reduction through photo-excited electrons (e-) in the ZnO (CB), which directly participate in CO2 reduction, leading to CO formation as follows (Reaction II)

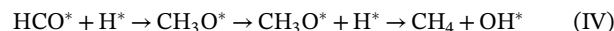


The key functional group for adsorbed CO2- [(2374 cm-1), (HT)] and bidentate/monodentate (CO3-) (1305 cm-1, 1310 cm-1) are present in both (WI) & (HT) [45, 46]. In a related mechanism, CO2 undergoes formate-mediated reduction wherein it forms a surface-bound formate species (HCOO\*) that subsequently decomposes to produce CO (2077 cm-1) as represented by Reaction (III) [47].



This pathway is supported by vibrational signatures corresponding to adsorbed O-C-O asymmetric stretch of HCO3- (1684 cm-1), (HT) as well as the asymmetric stretches of formate and carbonyl groups at (1593 cm-1) and (1753-1719 cm-1), respectively [48].

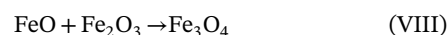
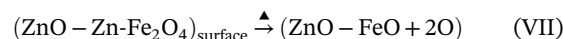
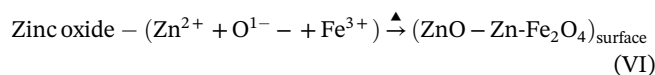
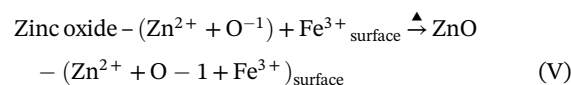
Furthermore, methane (CH4) generation occurs exclusively with the (HT) catalyst, emerging as a secondary product via successive hydrogenation steps. This process involves the formation of methoxy species from the hydrogenation of a formyl intermediate (HCO), as indicated by bands at (2927 and 2885 cm-1), and proceeds through subsequent surface reactions leading to CH4 formation (Reaction IV) [49, 50].



Additionally, possible bending vibrations of adsorbed H2O (1637 cm-1) and hydroxyl (-OH) vibrations from adsorbed H2O (3505, 3327, 3177 cm-1) in both (HT) and (WI) were observed [51]. Finally, the (WI) catalyst primarily produces CO, while the (HT) catalyst generates both CO and trace amounts of methane.

### 3.2.3 | Secondary Phase Formation

In the formation of surface-bound Fe3O4 in (WI) samples, it is suggested that thermal decomposition of Fe3+ precursor is a nitrate (as used for synthesis); thermal treatment (calcination) induces disproportionation or partial reduction. This pathway is common in oxygen-limited environments or when ZnO alters the local oxidation potential. This suggests the cause for forming Fe3O4, as shown in Reactions (V)-(VII) and Figure 9a-c [32, 52].



Iron loading through the (HT) method, as illustrated in Figure 9d-f, shows both bare ZnO and Fe-ZnO (4%). The absence of new phase formation is confirmed by XRD and XPS, indicating the successful incorporation of iron into the lattice of the ZnO. However, when the iron loading reaches 10% in Fe-ZnO, a new ZnFe2O4 phase emerges [53].

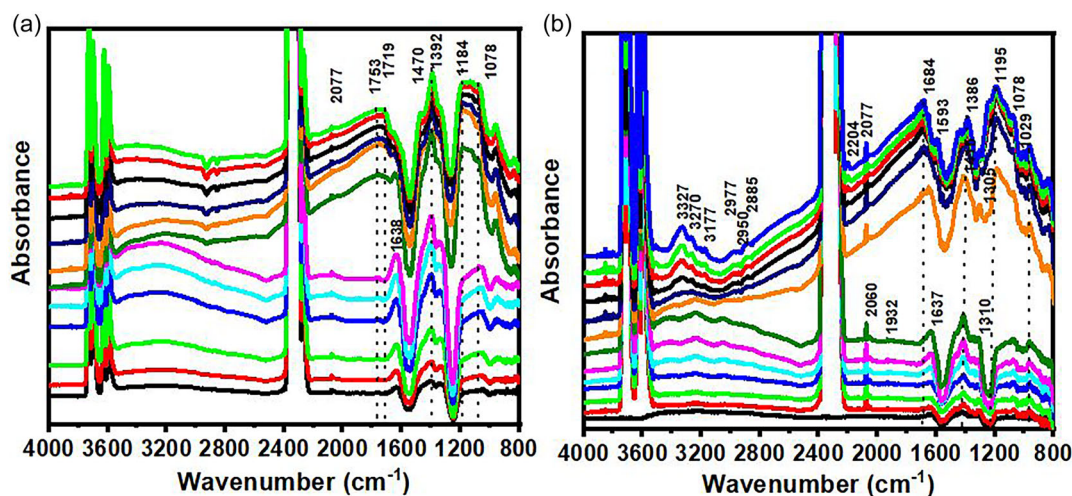
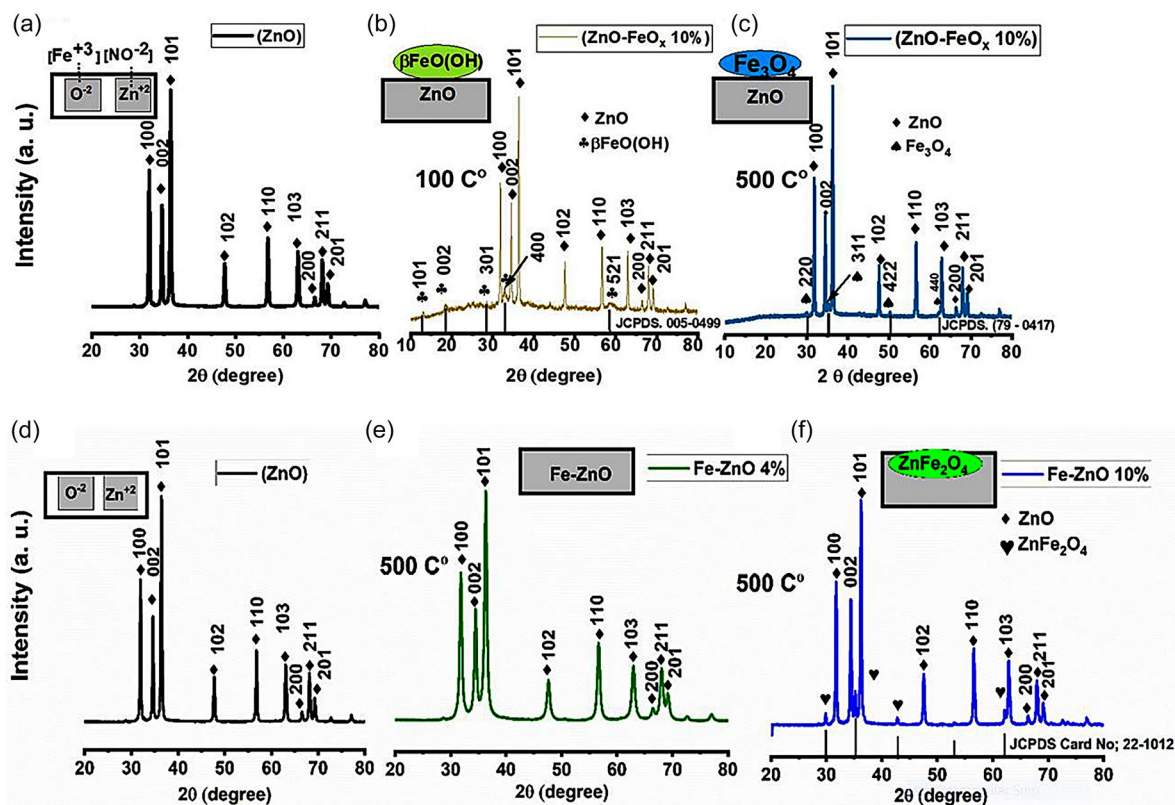


FIGURE 8 | DRIFTS spectra of (a) ZnO-FeOx sample (WI) and (b) ZnO-FeOx sample (HT).



**FIGURE 9** | The formation of a heterostructure of different temperature treatments (a–c) ZnO-FeO<sub>x</sub> samples via (WI) and (d–f) The formation of a new secondary phase due to iron loading by (HT) ZnFe<sub>2</sub>O<sub>4</sub>.

### 3.2.4 | DFT Calculation

The DFT-calculated band structure and DOS results correlate well with the experimental charge–transfer behavior. Pristine ZnO shows a calculated bandgap of ~3.3 eV, whereas Fe-doped ZnO exhibits an apparent bandgap narrowing to ~3.0 eV due to the emergence of Fe-3d-derived acceptor states just above the valence-band maximum (VBM) [54]. These Fe-related states introduce shallow hole-trapping centers that enhance spatial separation of photogenerated charge carriers. This agrees with the experimentally observed suppression of e<sup>-</sup>/h<sup>+</sup> recombination and the corresponding improvement in CO<sub>2</sub> photoreduction activity. The Fe-induced electronic states also modify the local electron density around Zn, enabling more efficient intra-lattice charge redistribution and utilization during catalysis. For ZnO-FeO<sub>x</sub> prepared via wet-impregnation, the calculated bandgap also decreases slightly (to ~3.1 eV), and Fe contributes electronic states near the conduction-band region. These states facilitate interfacial charge transport, consistent with the increased photocatalytic activity relative to pristine ZnO. Collectively, these results confirm that Fe incorporation either via lattice doping or enhanced charge transport across the ZnO-FeO<sub>x</sub> junction by introducing intermediate electronic states, reducing the effective bandgap, and mitigating recombination, thereby improving CO<sub>2</sub> activation and conversion efficiency.

## 4 | Conclusion

Iron incorporation into ZnO via both wet impregnation and hydrothermal methods led to bandgap narrowing and the introduction of impurity states, which suppressed charge carrier recombination

and enhanced photoactivity. The (WI) promoted the formation of iron oxides on the ZnO surface, facilitating effective charge separation through heterojunction formation, as confirmed by Kelvin probe spectroscopy. The ZnO-FeO<sub>x</sub> (8%) sample demonstrated the highest photocatalytic performance under UV light, achieving 99.99% CO selectivity, as supported by in situ DRIFTS analysis. In contrast, (HT) doped Fe-ZnO samples exhibited methane by-products and intermediate species such as carbonyls and formates. Although both approaches improved performance over pure ZnO, the (WI) method showed superior CO selectivity and photocatalytic activity, likely due to the presence of surface accessible active sites and partial interaction with the underlying ZnO lattice. Further in-depth studies focusing on the surface properties and photocatalytic mechanisms of (WI) systems are recommended.

### Acknowledgments

AS gratefully acknowledges the support of FK 143583, and ZK is grateful for the K21 138714 project from the source of the National Research, Development and Innovation Fund. The Ministry of Human Capacities through the 20391-3/2018/FEKUSSTRAT, as well as Project no. TKP2021-NVA-19 under the TKP2021-NVA funding scheme of the Ministry for Innovation and Technology, are acknowledged. Project no. RRF-2.3.1-21-2022–00009, titled (National Laboratory for Renewable Energy), has been implemented with the support provided by the Recovery and Resilience Facility of the European Union within the framework of Programme Széchenyi Plan Plus.

### Conflicts of Interest

The authors declare no conflicts of interest.

## Data Availability Statement

The data that support the findings of this study are available from the corresponding author upon reasonable request.

## References

1. D. R. Whang and D. H. Apaydin, "Artificial Photosynthesis: Learning From Nature," *ChemPhotoChem* 2 (2018): 148–160.
2. J. Barber, "Photosynthetic Energy Conversion: Natural and Artificial," *Chemical Society Reviews* 38 (2009): 185–196.
3. S. Wang, X. Han, Y. Zhang, N. Tian, T. Ma, and H. Huang, "Inside-and-Out Semiconductor Engineering for CO<sub>2</sub> Photoreduction: From Recent Advances to New Trends," *Small Structures* 2 (2021): 2000061.
4. T.-D. Hoang, S. A. Bandh, F. A. Malla, et al., "Carbon-Based Synthesized Materials for CO<sub>2</sub> Adsorption and Conversion: Its Potential for Carbon Recycling," *Recycling* 8 (2023): 53.
5. S. T. Janaki, D. K. Madheswaran, G. Naresh, and T. Praveenkumar, "Beyond Fossil: The Synthetic Fuel Surge for a Green-Energy Resurgence," *Clean Energy* 8 (2024): 1–19.
6. J. Qiao, Y. Liu, F. Hong, and J. Zhang, "A Review of Catalysts for the Electroreduction of Carbon Dioxide to Produce Low-Carbon Fuels," *Chemical Society Reviews* 43 (2014): 631–675.
7. D. Pan, Y. Wang, Q. Liang, et al., "Recent Advances in Solar-Driven Photothermal Nanostructured Materials for CO<sub>2</sub> Reduction: A Review," *Journal of Environmental Chemical Engineering* 11 (2023): 110324.
8. M. González-Castaño, B. Dorneanu, and H. Arellano-García, "The Reverse Water Gas Shift Reaction: A Process Systems Engineering Perspective," *Reaction Chemistry & Engineering* 6 (2021): 954–976.
9. C. Mebrahtu, F. Krebs, S. Perathoner, S. Abate, G. Centi, and R. Palkovits, "CO<sub>2</sub> Methanation: Principles and Challenges," in *Studies in Surface Science and Catalysis* (Elsevier, 2019), 85–103.
10. M. E. Dry, "The Fischer-Tropsch Process: 1950–2000," *Catalysis Today* 71 (2002): 227–241.
11. S. Balu, H. Venkatesvaran, K. W. Lan, and T. C.-K. Yang, "Synthesis of Highly Efficient (0D/1D) Z-Scheme CdS-NPs@ ZnO-NRs Visible-Light-Driven Photo (electro) Catalyst for PEC Oxygen Evolution Reaction and Removal of Tetracycline," *Catalysts* 12 (2022): 1601.
12. D. R. Paul, S. Gautam, P. Panchal, S. P. Nehra, P. Choudhary, and A. Sharma, "ZnO-Modified g-C<sub>3</sub>N<sub>4</sub>: A Potential Photocatalyst for Environmental Application," *ACS Omega* 5 (2020): 3828–3838.
13. R. Shah, D. Khan, A. Al-Anazi, et al., "Non-Metal Doped ZnO and TiO<sub>2</sub> Photocatalysts for Visible Light Active Degradation of Pharmaceuticals and Hydrogen Production: A Review," *Applied Catalysis O: Open* 204 (2025): 207043.
14. A. Baig, M. Siddique, and S. Panchal, "A Review of Visible-Light-Active Zinc Oxide Photocatalysts for Environmental Application," *Catalysts* 15 (2025): 100.
15. M. Archi, L. Moulouai, M. Karouchi, et al., "First-Principles Study of Co-Doped Wurtzite ZnO: Insights into Carrier Dynamics, Visible Light Absorption, and Structural Properties for Solar Cell Applications," *Optical and Quantum Electronics* 57 (2025): 269.
16. Q. Lin, R. Zhang, X. Zhang, et al., "Electrospun Fiber Membranes of Fe<sub>2</sub>O<sub>3</sub>/ZnO with High Photocatalytic Activity for Wastewater Treatment Application under Visible Light Irradiation," *Catalysis Letters* 155 (2025): 67.
17. P. Dhiman, G. Rana, A. Kumar, G. Sharma, D.-V. N. Vo, and M. Naushad, "ZnO-Based Heterostructures as Photocatalysts for Hydrogen Generation and Depollution: A Review," *Environmental Chemistry Letters* 20 (2022): 1047–1081.
18. Z. Luo, C. P. Leo, F. Guo, and X. Zhao, "Visible Light Initiated Norfloxacin Degradation through a Double Z-Scheme Bi<sub>2</sub>WO<sub>6</sub>/ZnO/CdS Photocatalyst," *Separation and Purification Technology* 366 (2025): 132670.
19. X. Ma, D. Li, Y. Jiang, et al., "Fiber-Like ZnO with Highly Dispersed Pt Nanoparticles for Enhanced Photocatalytic CO<sub>2</sub> Reduction," *Journal of Colloid and Interface Science* 628 (2022): 768–776.
20. L. Yuan, M. Y. Qi, Z. R. Tang, and Y. J. Xu, "Coupling Strategy for CO<sub>2</sub> Valorization Integrated with Organic Synthesis by Heterogeneous Photocatalysis," *Angewandte Chemie* 60 (2021): 21150–21172.
21. Y. Zhang, C.-L. Tan, Y.-J. Xu, and Z.-R. Tang, "Emerging Platform and Frontier of Upcycling Plastic Waste by Regulating Photoredox Half-Reactions," *Molecular Catalysis* 588 (2026): 115545.
22. Y. Zhang, L.-H. Gao, M.-Y. Qi, Z.-R. Tang, and Y.-J. Xu, "Cooperative Photoredox Coupling of CO<sub>2</sub> Reduction with Thiols Oxidation by Hybrid CdSe/CdS Semiconductor Quantum Dots," *Applied Catalysis B: Environment and Energy* 367 (2025): 125118.
23. H.-L. Wu, M. Y. Qi, C. L. Tan, Y. Zhang, Z.-R. Tang, and Y.-J. Xu, "Selective Photoredox Enabled C-C Coupling of Ethanol over Pt-Modified ZnO. 75CdO. 25S Catalyst," *ACS Materials Letters* 7 (2025): 3111–3119.
24. M. Salem, A. Haouas, J. Salem, R. Daoub, and M. Gassoumi, "Synthesis and Characterization of Fe, Cu, and Cr Doped ZnO Nanocrystallite Films and the Effects on Passivation of Silicon Surface," *Silicon* 16 (2024): 4729–4738.
25. H. Zhang, D. Yang, X. Ma, S. Li, and D. Que, "Controllable Growth of ZnO Nanostructures by Citric Acid Assisted Hydrothermal Process," *Materials Letters* 59 (2005): 1696–1700.
26. P. Giannozzi, S. Baroni, N. Bonini, et al., "QUANTUM ESPRESSO: A Modular and Open-Source Software Project for Quantum Simulations of Materials," *Journal of Physics: Condensed Matter* 21 (2009): 395502.
27. Y. Yao, Y. Gao, L. Ye, H. Chen, and L. Sun, "Highly Efficient Photocatalytic Reduction of CO<sub>2</sub> and H<sub>2</sub>O to CO and H<sub>2</sub> with a Cobalt Bipyridyl Complex," *Journal of Energy Chemistry* 27 (2018): 502–506.
28. L. Fang, B. Zhang, W. Li, X. Li, T. Xin, and Q. Zhang, "Controllable Synthesis of ZnO Hierarchical Architectures and Their Photocatalytic Property," *Superlattices and Microstructures* 75 (2014): 324–333.
29. W. Bousslama, H. Elhouichet, and M. Férid, "Enhanced Photocatalytic Activity of Fe Doped ZnO Nanocrystals under Sunlight Irradiation," *Optik* 134 (2017): 88–98.
30. P. Kumar, A. Gaur, and R. Kotnala, "Magneto-Electric Response in Pb Substituted M-Type Barium-Hexaferrite," *Ceramics International* 43 (2017): 1180–1185.
31. M. Zhang, F. Averseng, J. M. Krafft, P. Borghetti, G. Costentin, and S. Stankic, "Controlled Formation of Native Defects in Ultrapure ZnO for the Assignment of Green Emissions to Oxygen Vacancies," *The Journal of Physical Chemistry C* 124 (2020): 12696–12704.
32. M. T. Qamar, M. Aslam, Z. A. Rehan, et al., "The Effect of Fe<sup>3+</sup> Based Visible Light Receptive Interfacial Phases on the Photocatalytic Activity of ZnO for the Removal of 2, 4-Dichlorophenoxy Acetic Acid in Natural Sunlight Exposure," *Separation and Purification Technology* 172 (2017): 512–528.
33. R. L. d. S. Silva and A. Franco Jr, "Raman Spectroscopy Study of Structural Disorder Degree of ZnO Ceramics," *Materials Science in Semiconductor Processing* 119 (2020): 105227.
34. M. Silambarasan, S. Saravanan, and T. Soga, "Raman and Photoluminescence Studies of Ag and Fe-Doped ZnO Nanoparticles," *International Journal of ChemTech Research* 7 (2015): 1644–1650.
35. C. Bundesmann, N. Ashkenov, M. Schubert, et al., "Raman Scattering in ZnO Thin Films Doped with Fe, Sb, Al, Ga, and Li," *Applied Physics Letters* 83 (2003): 1974–1976.

36. K. J. Archana, A. C. Preetha, and K. Balasubramanian, "Influence of Urbach Energy in Enhanced Photocatalytic Activity of Cu Doped ZnO Nanoparticles," *Optical Materials* 127 (2022): 112245.
37. L. Gu, X. Cao, A. Mukhtar, and K. Wu, "Structural Characterization and Magnetic Properties of Core-Shell Fe@Fe<sub>3</sub>O<sub>4</sub> Nanowires," *Applied Physics A* 126 (2020): 458.
38. A. P. Grosvenor, M. C. Biesinger, R. S. C. Smart, and N. S. McIntyre, "Investigation of Multiplet Splitting of Fe 2p XPS Spectra and Bonding in Iron Compounds," *Surface and Interface Analysis* 36 (2004): 1564–1574.
39. Z. Wang, J. Lu, S. Cheng, J. Ye, M. Yi, and J. Shen, "Performance, Mechanism, and Ecotoxicity Assessment of Sulfamethoxazole Degradation by Coupling Visible-Light Photocatalysis with Persulphate Activation over Fe<sub>3</sub>O<sub>4</sub>/ZnO Composites," *International Journal of Environmental Analytical Chemistry* 104 (2024): 1–18.
40. D. Channei and S. Phanichphant, "Fe<sub>3</sub>O<sub>4</sub>/SiO<sub>2</sub>/CeO<sub>2</sub> Core-Shell Magnetic Nanoparticles as Photocatalyst," *Journal of Nanoscience and Nanotechnology* 14 (2014): 7756–7762.
41. J. Zhou, X. Lyu, X. Xia, J. Ma, L. Yan, and B. Gao, "A Mini-Review of Functionalized Magnetic Fe<sub>3</sub>O<sub>4</sub> Nanoparticles: From Fundamentals to Application," *Boletín De LA Sociedad Española De Cerámica y Vidrio* 64 (2025): 1–22.
42. S. R. Morrison, "The Solid/Liquid Interface," in *The Chemical Physics of Surfaces* (Springer, 1980), 297–331.
43. R. Vishnuraj, K. K. Karuppanan, M. Aleem, and B. Pullithadathil, "Boosting the Performance of NO<sub>2</sub> Gas Sensors Based on n-n Type Mesoporous ZnO@In<sub>2</sub>O<sub>3</sub> Heterojunction Nanowires: In Situ Conducting Probe Atomic Force Microscopic Elucidation of Room Temperature Local Electron Transport," *Nanoscale Advances* 2 (2020): 4785–4797.
44. X. An, H. Ding, Y. Wang, et al., "Microwave-Assisted One-Step Synthesis of Fe<sub>3</sub>O<sub>4</sub>/ZnO@MXene Multi-Dimensional Composite for Photocatalysis and Electromagnetic Wave Absorption," *Applied Surface Science* 669 (2025): 163532.
45. G. Zhang, Z. Wang, and J. Wu, "Construction of a Z-Scheme Heterojunction for High-Efficiency Visible-Light-Driven Photocatalytic CO<sub>2</sub> Reduction," *Nanoscale* 13 (2021): 4359–4389.
46. H. Li, B. Yang, H. Kong, J. Zhao, and Q. Cai, "Magnetic CoNi@N-Doped Carbon Composite for CO<sub>2</sub> Electrochemical Reduction to CH<sub>4</sub> Associated with Methanol Oxidation to Methylal in an Ionic Liquid Electrolyte," *Industrial & Engineering Chemistry Research* 64 (2024): 113–122.
47. F. Villagra-Soza, S. Godoy, A. Karelavic, and R. Jiménez, "Scrutinizing the Mechanism of CO<sub>2</sub> Hydrogenation over Ni, CO and Bimetallic NiCo Surfaces: Isotopic Measurements, Operando-FTIR Experiments and Kinetics Modelling," *Journal of Catalysis* 414 (2022): 1–15.
48. L.-Y. Lin, C. Liu, and T.-T. Hsieh, "Efficient Visible and NIR Light-Driven Photocatalytic CO<sub>2</sub> Reduction over Defect-Engineered ZnO/Carbon Dot Hybrid and Mechanistic Insights," *Journal of Catalysis* 391 (2020): 298–311.
49. F. Romero-Sarria, L. F. Bobadilla, E. J. Barrera, and J. A. Odriozola, "Experimental Evidence of HCO Species as Intermediate in the Fischer Tropsch Reaction Using Operando Techniques," *Applied Catalysis B: Environmental* 272 (2020): 119032.
50. I. Luisetto, S. Stendardo, S. M. Senthil Kumar, et al., "One-Pot Synthesis of Ni<sub>0.05</sub>Ce<sub>0.95</sub>O<sub>2-δ</sub> Catalysts with Nanocubes and Nanorods Morphology for CO<sub>2</sub> Methanation Reaction and in Operando DRIFT Analysis of Intermediate Species," *Processes* 9 (2021): 1899.
51. M. Takeuchi, G. Martra, S. Coluccia, and M. Anpo, "Investigations of the Structure of H<sub>2</sub>O Clusters Adsorbed on TiO<sub>2</sub> Surfaces by Near-Infrared Absorption Spectroscopy," *The Journal of Physical Chemistry B* 109 (2005): 7387–7391.
52. K. Tanji, J. A. Navio, A. N. Martín-Gómez, et al., "Role of Fe (III) in Aqueous Solution or Deposited on ZnO Surface in the Photoassisted Degradation of Rhodamine B and Caffeine," *Chemosphere* 241 (2020): 125009.
53. A. Esbergenova, M. Hojamberdiev, Z. C. Kadirova, et al., "Interlinking the Fe Doping Concentration, Optoelectronic Properties, and Photocatalytic Performance of ZnO Nanostructures," *Current Applied Physics* 67 (2024): 18–29.
54. Z. Ma, C. Luo, C. Wang, and J. Liu, "Study of Optical Properties of ZnO Doped with Fe," *Optik* 188 (2019): 104–109.

### Supporting Information

Additional supporting information can be found online in the Supporting Information section. **Supporting Fig. S1:** EDS mapping for ZnO-FeO<sub>x</sub> 8% wet impregnation (a-d), Fe-ZnO 4% hydrothermal (e-h). **Supporting Fig. S2:** Raman shift for ZnO-FeO<sub>x</sub> wet impregnated method (WI). **Supporting Fig. S3:** Raman shift for Fe-ZnO doped hydrothermal method (HT). **Supporting Fig. S4:** XPS spectra for Zn 2p wet ZnO pure (a), Zn modified auger ZnO pure (b), O1 wet impregnated (c), O1 hydrothermal (d), Zn 2p wet impregnated (e), Zn 2p hydrothermal (f) Zn modified auger wet and hydrothermal (f&h) C1 (i) for wet and (j) for hydrothermal. **Supporting Fig. S5:** Bulk model ZnO pure (a), Fe 4% Fe doped (b), for wet impregnated sample. Band structure and density of states for ZnO pure (d & e), for 4% Fe doping (f & g), for ZnO-FeO<sub>x</sub> wet impregnated sample (h & i). **Supporting Fig. S6:** CO selectivity for ZnO - Fe loaded via (hydrothermal wet impregnation) using UV and visible irradiation. **Supporting Fig. S7:** CO Yield recycle ZnO - Fe loaded via (hydrothermal wet impregnation) using uv and visible irradiation. **Supporting Fig. S8:** TGA plot for ZnO-FeO<sub>x</sub> (a) (WT) sample before reaction, (WT) after reaction. **Supporting Fig. S9:** Urbach Energy (ln(α) vs hν) for Fe-ZnO Hydrothermal method. **Supporting Table S1:** ZnO and Fe loading ZnO Optical properties. **Supporting Table S2:** Urbach Energy for Fe -ZnO (HT). **Supporting Table S3:** Fe XPS Analysis. **Supporting Table S4:** Zn & modified Auger parameter. **Supporting Table S5:** Comparison ZnO samples with the previous literature towards photocatalytic CO<sub>2</sub> reduction under certain reaction conditions.